# Supplementary Material for
# β-adrenergic effects on cardiac myofilaments and contraction in an integrated rabbit ventricular myocyte model

Negroni, Morotti, Lascano, Gomes, Grandi, Puglisi and Bers

## *Parallel elastic element*

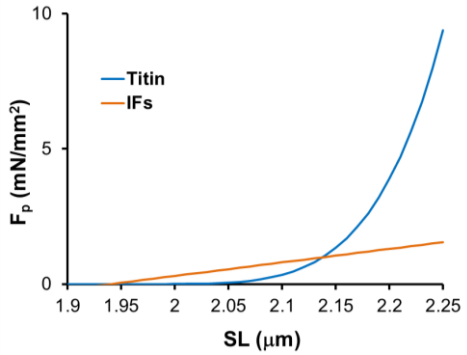


**Fig. S1**. Force ($F_p$) response as a function of sarcomere length (SL) of the non-linear (representing titin) and linear (IFs, representing cellular passive elements) components of the parallel elastic element, similar to the constituents identified in Fig. 7 of Granzier *et al*. [1].

## *Updates to Soltis-Saucerman model*

Several updates were made to the parent Soltis-Saucerman model [2] (for PKA signaling).

- ***Phospholemman***

PKA-dependent modulation of PLM was modeled as previously done in [3, 4]. The total protein concentration was set to the value of 48 μmol/L cytosol. 100 nM [ISO] administration sensitizes NKA to $[Na^+]_i$ by increasing the NKA affinity for internal $Na^+$ ($K_{mNaip}$ is reduced from 11 to 8 mM).

$fracPKA\_PLMo = 0.006294$ ; *derived quantity*

$fracPKA\_PLMiso = 0.9232$ ; *derived quantity*

$$kPKA\_PLM = \frac{11\ (1 - 0.7019)}{\frac{fracPKA\_PLMiso}{fracPKA\_PLMo} - 1}\ ;$$

$$KmNaip\_PKA = -\ kPKA\_PLM + kPKA\_PLM\ \frac{PLM\_PKAp}{fracPKA\_PLMo}\ ;$$

$K_{mNaip} = 11 - KmNaip\_PKA$ . *[mM]*

- ***$I_{Ks}$***

The rate constants of $I_{Ks}$ phosphorylation and dephosphorylation were respectively changed from the original values of 54 and 8.52 $s^{-1}$ to 1.87 and 0.19 $s^{-1}$, as in [4].

- ***$I_{Kr}$***

PKA-dependent modulation of $I_{Kr}$ was modeled with same extent and kinetics of $I_{Ks}$ phosphorylation, as in [5]. Total protein concentration was set to 0.025 μmol/L cytosol. 100 nM [ISO] administration increases $I_{Kr}$ conductance by 30% and causes a 10 mV leftward shift in the current-voltage relationship.

$fracPKA\_IKro = 0.1098$ ; *derived quantity*

$fracPKA\_IKriso = 0.8380$ ; *derived quantity*

$$kPKA\_IKr = \frac{PLM\_IKrp - fracPKA\_IKro}{fracPKA\_IKriso - fracPKA\_IKro}\ ;$$

$G_{Kr} = (1 + 0.3\ kPKA\_IKr)\ 0.003\ \sqrt{[K^+]_o/5.4}$ ; *[nS $pF^{-1}$]*

$V_{shift} = 10\ \ kPKA\_IKr$ . *[mV]*

- ***$I_{Cl(Ca)}$***

PKA-dependent modulation of $I_{Cl(Ca)}$ was modeled with same extent and kinetics of CFTR-mediated $Cl^-$ current phosphorylation. Total protein concentration was 0.025 μmol/L cytosol. 100 nM [ISO] administration increases channel $Ca^{2+}$-affinity by reducing the parameter $K_{dClCa}$ by 30%.

$fracPKA\_IClCao = 0.1624$ ; *derived quantity*

$fracPKA\_IClCaiso = 0.8918$ ; *derived quantity*

$$kPKA\_IClCa = \frac{PLM\_IClCap - fracPKA\_IClCao}{fracPKA\_IClCaiso - fracPKA\_IClCao}\ ;$$

$K_{dClCa} = (1 + (0.704 - 1)\ kPKA\_IClCa)\ 100e\text{-}3$ . *[mM]*

- ***Myofilament***

PKA-dependent modulation of myofilament was modeled with same extent and kinetics of troponin I phosphorylation. We assumed the same total concentration as well (70 μmol/L cytosol). 100 nM [ISO] administration reduces myofilament stiffness and XBCa, and increases XBcy.

$fracPKA\_Myoo = 0.1624$ ; *derived quantity*

$fracPKA\_Myoiso = 0.8918$ ; *derived quantity*

$$kPKA\_Myo = \frac{PLM\_Myop - fracPKA\_IMyoo}{fracPKA\_IMyoiso - fracPKA\_IMyoo};$$

$K_e$ = (1 + (0.5 - 1) *kPKA_Myo*) 105000 ; $[mN\ mm^{-2}\ \mu m^{-5}]$

$Z_b$ = (1 + (4.2 - 1) *kPKA_Myo*) 0.1397 ; $[ms^{-1}]$

$Z_r$ = (1 + (1.8 - 1) *kPKA_Myo*) 7262.6e6 ; $[mM^{-3}\ ms^{-1}]$

$Y_r$ = (1 + (2.2 - 1) *kPKA_Myo*) 0.1397 ; $[ms^{-1}]$

$Z_a$ = (1 + (1.24 - 1) *kPKA_Myo*) 0.0023 ; $[ms^{-1}]$

$f$ = (1 + (1.24 - 1) *kPKA_Myo*) 0.0023 ; $[ms^{-1}]$

*RLa* = (1 + (0.4 - 1) *kPKA_Myo*) 20 ; $[\mu m^{-2}]$

$Z_p$ = (1 + (2.2 - 1) *kPKA_Myo*) 0.2095 ; $[ms^{-1}]$

$Y_p$ = (1 + (2.2 - 1) *kPKA_Myo*) 0.1397 ; $[ms^{-1}]$

$B_p$ = (1 + (3.4 - 1) *kPKA_Myo*) 0.5 ; $[ms^{-1}]$

$B_w$ = (1 + (3.4 - 1) *kPKA_Myo*) 0.35 ; $[ms^{-1}]$

$Y_c$ = (1 + (0.4 - 1) *kPKA_Myo*) 4 ; $[\mu m^{-1}]$

$Y_d$ = (1 + (2.2 - 1) *kPKA_Myo*) 0.028 ; $[ms^{-1}]$

$Y_v$ = (1 + (1.6 - 1) *kPKA_Myo*) 0.9 . $[ms^{-1}]$

## *ISO effect on ion currents and transporters*

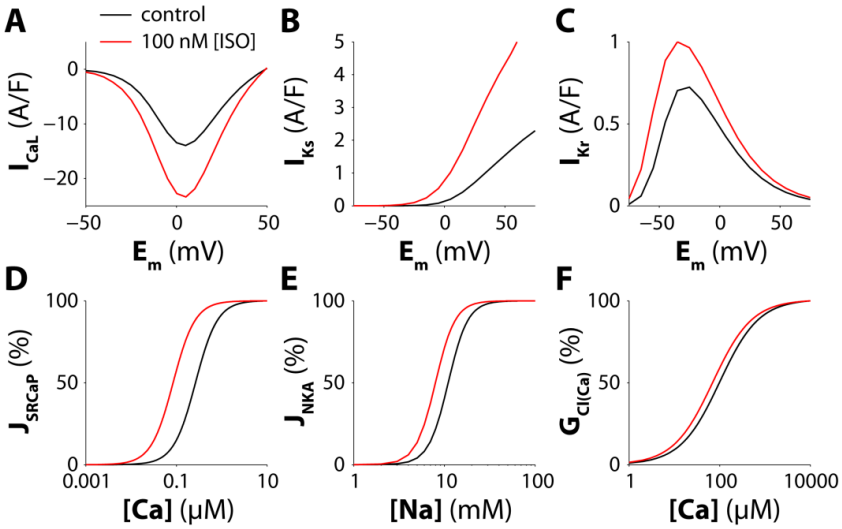


**Fig. S2.** Effects of β-AS (100 nM [ISO]) on myocyte ion currents and transporters. Peak I-V relationships for $I_{CaL}$ (**A**), $I_{Ks}$ (**B**) and $I_{Kr}$ (**C**). **D**: normalized maximal $J_{SRCaP}$ as a function of $[Ca^{2+}]_i$ at constant $[Ca^{2+}]_{SR}$ (0.55 mM). **E**: normalized maximal $J_{NKA}$ as a function of $[Na^+]_i$. **F**: normalized maximal $Ca^{2+}$-dependent $Cl^-$ channel conductance as a function of $[Ca^{2+}]_i$.

## *ISO effect on titin*

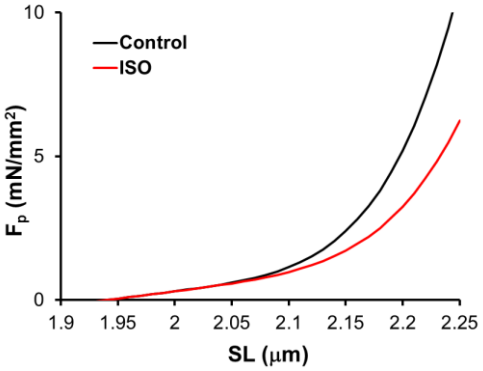


**Fig. S3.** ISO effect on total parallel elastic force ($F_p$). ISO (100 nM) effect on titin was simulated by reducing titin stiffness by 50%. In isometric twitches simulated at 1.05 μm half-sarcomere length (2.1 μm sarcomere length), this action in conjunction with ISO effects on other targets, reduced passive force [$F_p$(min)] 14.5% from 0.9 to 0.77 $mN.mm^{-2}$, within the range of experimental diastolic force change (20%) in stimulated intact rat ventricular trabeculae (see Fig. 7B of Fukuda *et al.* [5]).

## *Action potential (AP) reconstruction and $Ca^{2+}$ fluxes*

In myocyte models, the AP is built by means of a differential equation involving all the transarcolemmal ion currents as described in detail by Shannon *et al.* [6], where there is a cleft, subsarcolemmal and cytosolic compartment (Fig. 1C of paper). The cleft and Sub-SL include all of the ionic currents that directly influence membrane potential ($E_m$). Relevant for $Ca^{2+}$ fluxes, the model places 90% of CaL channels in the cleft, and 10% in the Sub-SL. NCX is assumed to be uniformly distributed in the sarcolemma, such that 11% is in the cleft and 89% in the Sub-SL. That is, the cleft region occupies 11% of the total sarcolemmal membrane. Most other sarcolemmal channels/transporters are, like NCX, evenly distributed throughout the sarcolemma (same density in cleft and Sub-SL). $Ca^{2+}$ entering via cleft $I_{CaL}$ and subsequently released from the SR elevates cleft $Ca^{2+}$ concentration ($[Ca^{2+}]_{CL}$). This diffuses to the Sub-SL space, which along with Sub-SL $I_{CaL}$ and NCX fluxes, Sub-SL $Ca^{2+}$ buffering and diffusion to the cytosolic bulk, determine $[Ca^{2+}]_{SL}$. The dynamics of $[Ca^{2+}]_{SL}$ vs. cytosolic $[Ca^{2+}]_i$ were constrained by measurements of $[Ca^{2+}]_{SL}$ sensed by the NCX during SR $Ca^{2+}$ release [6, 7]. That is, $[Ca^{2+}]_{SL}$ reaches a several-fold higher peak than $[Ca^{2+}]_i$. The relative amplitude and kinetics of cleft, Sub-SL and cytosolic $[Ca^{2+}]_i$ can be seen in Fig. S4.

Fig. S2 summarizes β-AS effects on its main ionic transport targets. In β-AS, $I_{CaL}$, $I_{Cl(Ca)}$, $I_{Kr}$ and $I_{Ks}$ are directly modified, but there are also indirect effects on $Ca^{2+}$-sensitive channels and transporters that are caused by higher local

$[Ca^{2+}]$. Together, these changes slightly shorten APD at steady-state. APD shortening is driven by increasing outward $I_{Ks}$ (as preventing the ISO-dependent $I_{Ks}$ effect prolongs APD, Fig. 5D in paper), but counteracted by an increase in $I_{CaL}$ (Fig. 5A) and the PLM-induced decrease in $[Na^+]_i$, which reduces repolarizing $I_{NKA}$ (Fig. 5C). Indeed, when the PLM effect is attenuated (at a lower [ISO], Fig. 7) to limit $[Na^+]_i$ unloading, APD shortens more markedly. When the ISO effect on PLM is eliminated (Fig. 5C) APD shortens.

Enhanced $I_{CaL}$ produces both increased and earlier rise in $[Ca^{2+}]_{CL}$ (from 77 to 228 µM in ISO and 278 µM in ISO-XBCa; Table 4 and Fig. S4A). The main reason that peak ISO-XBCa $[Ca^{2+}]_{CL}$ is 18% higher is secondary to the enhanced cytosolic $Ca^{2+}$ buffering (by TnI) which reduces $[Ca^{2+}]_i$ (and to a very slight extent $[Ca^{2+}]_{SL}$). That lower $[Ca^{2+}]_i$ results in less $Ca^{2+}$ extrusion via NCX, resulting in a small steady state increase in diastolic $[Ca^{2+}]_{SR}$ (by 3%). That higher $[Ca^{2+}]_{SR}$ is sufficient to increase SR $Ca^{2+}$ release flux, which is why the ISO-XBCa curve peak in Fig. S4A is slightly higher than for ISO. If we prevent this slow rise in SR $Ca^{2+}$, the red and green curves in Fig S4A are absolutely identical and for Fig S4B they are very nearly identical until ~50ms.

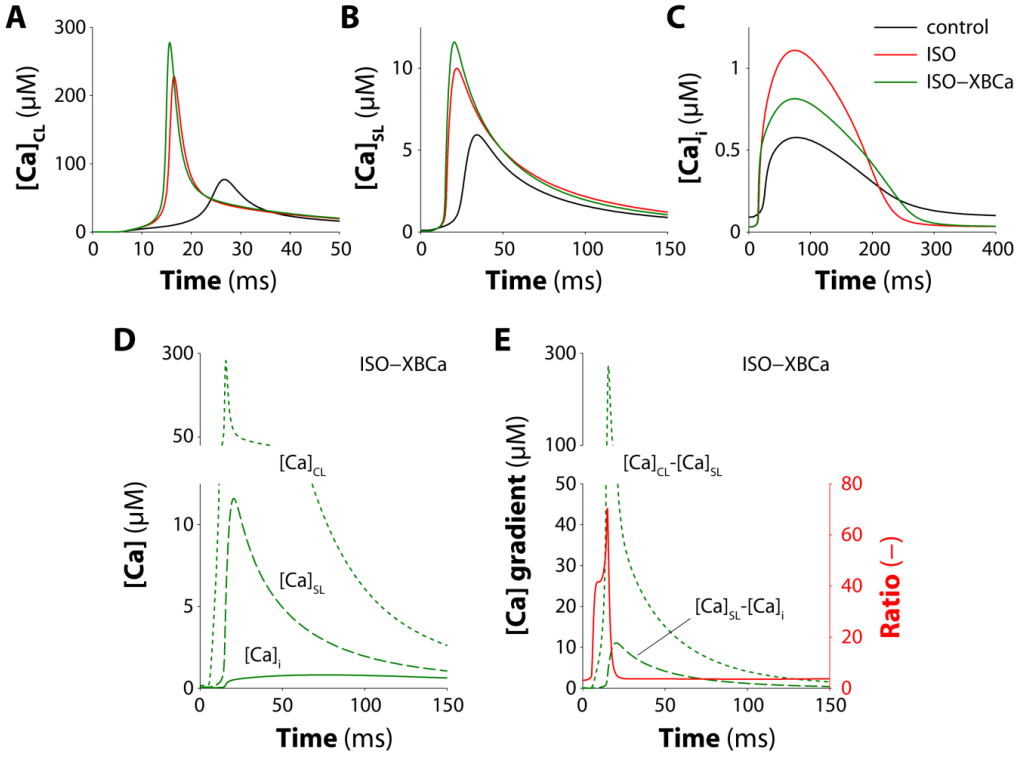


**Fig. S4**: Cleft $[Ca^{2+}]$ ($[Ca]_{CL}$, panel **A**), Sub-SL space $[Ca]_i$ ($[Ca]_{SL}$, **B**), and cytosolic $[Ca^{2+}]_i$ (**C**) during steady state twitches in **control**, **ISO** and **ISO-XBCa** (100 nM [ISO]). XBCa makes little difference in $[Ca^{2+}]_{CL}$ or $[Ca^{2+}]_{SL}$, despite major difference in $[Ca^{2+}]_i$. Higher peak $[Ca^{2+}]_{CL}$ and $[Ca^{2+}]_{SL}$ for ISO-XBCa is due to higher SR $Ca^{2+}$ load and release (see text above). **D**. Superimposed $[Ca^{2+}]_{CL}$, $[Ca^{2+}]_{SL}$ and $[Ca^{2+}]_i$ and gradients (**E**) from ISO-XBCa in A-C. The ratio between the two gradients is in red in **E**, indicating dominance of the $[Ca^{2+}]_{CL}$–$[Ca^{2+}]_{SL}$ gradient (flux from cleft to Sub-SL) vs. flux out of Sub-SL in controlling $[Ca^{2+}]_{SL}$, until net release stops (peak of $[Ca^{2+}]_{CL}$–$[Ca^{2+}]_{SL}$ and rapid ratio fall).

Fig. S4 also explains the somewhat surprising result that the smaller peak $[Ca^{2+}]_i$ in ISO-XBCa vs. ISO results in an almost unaltered AP shape and duration. Fig. S4D shows $[Ca^{2+}]_{CL}$, $[Ca^{2+}]_{SL}$ and $[Ca^{2+}]_i$ on a single graph for the ISO-XBCa case. During $I_{CaL}$ and SR $Ca^{2+}$ release, $[Ca^{2+}]_{CL}$ is very high and virtually uninfluenced by TnC $Ca^{2+}$ buffering. Rather, $[Ca^{2+}]_{CL}$ depends almost entirely on $Ca^{2+}$ fluxes into the cleft, cleft $Ca^{2+}$ buffering and diffusion out to the Sub-SL (and extrusion by cleft NCX). The Sub-SL space (containing all non-cleft $Ca^{2+}$-sensitive channels and transporters) is only somewhat less isolated from the myofilaments. That is, $[Ca^{2+}]_{CL}$ drives up $[Ca^{2+}]_{SL}$ (and that flux is unaltered by myofilaments), while diffusion from Sub-SL to cytosol (driven by $[Ca^{2+}]$ gradient $[Ca^{2+}]_{SL}$–$[Ca^{2+}]_i$) is only slightly accelerated by lower $[Ca^{2+}]_i$. As release shuts off (peak of $[Ca^{2+}]_{CL}$–$[Ca^{2+}]_{SL}$ curve in Fig. S4E), $[Ca^{2+}]_{SL}$ is progressively less dominated by $[Ca^{2+}]_{CL}$ and the green curve in Fig. S4B gradually falls below the red curve at ~50 ms). This is because the driving force (or gradient) $[Ca^{2+}]_{CL}$–$[Ca^{2+}]_{SL}$ falls steeply and that of $[Ca^{2+}]_{SL}$–$[Ca^{2+}]_i$ is near its peak (Fig. S4E). At that point, diffusion from Sub-SL to cytosol has a relatively stronger impact on $[Ca^{2+}]_{SL}$ (i.e. the ratio of $[Ca^{2+}]$ gradients drops from ~70× to 3×). That is, $[Ca^{2+}]_{SL}$ changes from being totally dominated by $[Ca^{2+}]_{CL}$ and is now more influenced by the driving force ($[Ca^{2+}]_{SL}$–$[Ca^{2+}]_i$).

The result is that the altered myofilament buffering has virtually no effect on cleft $Ca^{2+}$ channels (including RyR and NCX) and only slight effects on non-cleft $Ca^{2+}$-dependent currents (mainly later in the $Ca^{2+}$ transient). That is why APD is almost unaltered by removing XBCa effect from ISO (ISO-XBCa). If we double the diffusion constants for $Ca^{2+}$ and $Na^+$ from Sub-SL to cytosol, then APD is still only slightly changed. In contrast, reducing the amount of SR $Ca^{2+}$ released, produces strong and relatively proportional decreases in $[Ca^{2+}]_{CL}$, $[Ca^{2+}]_{SL}$ and $[Ca^{2+}]_i$ (and $I_{CaL}$ inactivation, $I_{NCX}$ and APD). Increasing these $Ca^{2+}$ fluxes, as with ISO, shows the converse, large increases in $[Ca^{2+}]$ in all of the compartments.

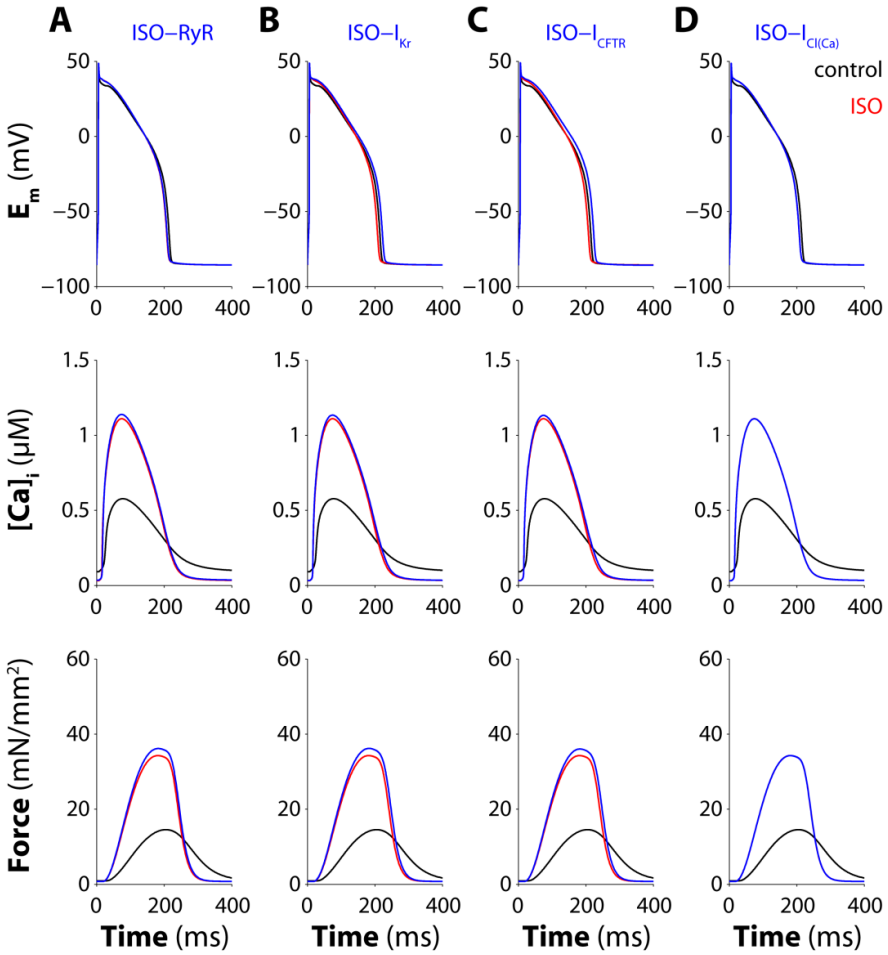


**Fig. S5.** Effects of PKA-dependent phosphorylation on isolated targets. Time courses of membrane potential (top), $[Ca^{2+}]_i$ (middle) and isometric force (bottom) during 1-Hz stimulation, before (black lines), after 100 nM [ISO] administration (red) or with ISO with the PKA effects selectively switched off at RyR (**A**), $I_{Kr}$ (**B**), CFTR (**C**), and $I_{Cl(Ca)}$ (**D**). This complements Fig. 5 that highlights PKA targets that have major effects on AP, $[Ca^{2+}]_i$ or force.

Table S1 below includes analysis values for data in Figs. 5 and S5, and is analogous to Table 4 in paper.

**Table S1.** Isometric twitch responses to ISO, ISO-$I_{CaL}$, ISO-PLB, ISO-PLM, and ISO-$I_{Ks}$.

| **Feature** | **Units** | **Control** | **ISO** | **ISO-$I_{CaL}$** | **ISO-PLB** | **ISO-PLM** | **ISO-$I_{Ks}$** |
|---|---|---|---|---|---|---|---|
| | | | **Isometric contractions** ($L_m$ = 1.05 μm) | | | | |
| $APD_{90}$ | ms | 211.3 | 204.3 | 170.7 | 204.6 | 188.3 | 240.6 |
| $[Ca^{2+}]_{CL}$(max) | μM | 77.0 | 228.4 | 64.3 | 122.3 | 322.5 | 280.9 |
| $[Ca^{2+}]_{SL}$(max) | μM | 5.94 | 10.00 | 4.38 | 7.02 | 13.36 | 11.72 |
| $[Ca^{2+}]_i$(max) | μM | 0.577 | 1.110 | 0.546 | 0.935 | 1.353 | 1.226 |
| $[Ca^{2+}]_i$(min) | μM | 0.091 | 0.031 | 0.027 | 0.085 | 0.034 | 0.033 |
| TCa(max) | ms | 77.3 | 75.4 | 68.5 | 74.9 | 78.3 | 74.8 |
| $TCa_{50}$ | ms | 114.6 | 105.6 | 57.4 | 102.0 | 120.5 | 118.0 |
| $TCa_{90}$ | ms | 213.2 | 157.2 | 90.1 | 180.4 | 186.8 | 178.5 |
| $F_m$(max) | mN $mm^{-2}$ | 14.5 | 34.3 | 4.14 | 22.6 | 55.6 | 43.7 |
| $F_m$(min) | mN $mm^{-2}$ | 0.91 | 0.76 | 0.76 | 0.78 | 0.76 | 0.76 |
| $TP_{50}$ | ms | 107.3 | 87.4 | 74.0 | 86.9 | 92.3 | 88.8 |
| $RT_{50}$ | ms | 93.4 | 66.2 | 37.3 | 76.4 | 78.2 | 77.8 |
| $T_{90}$ | ms | 378.5 | 280.7 | 193.7 | 293.3 | 313.1 | 300.8 |

## *Titin contribution to restoring force*

Although twitches were simulated at a larger sarcomere length (2.1 µm) than the range at which restoring force has been measured (1.6-1.9 µm), sarcomere restoring force was calculated to test whether twitch results contradicted the observed contribution of titin to this force. Fig. S6A shows restoring force simulations represented as sarcomere length at peak contraction ($SL_{PC}$) as a function of maximum relengthening velocity ($dL/dt_{max}$) following step changes in pCa according to Helmes *et al.* [8], since the experimental method to measure restoring force (ATP relaxing solution following ATP-free rigor contractions) could not be reproduced in the model because it does not contemplate ATP management. The figure shows the control relationship and after applying 50% reduction to titin stiffness. It can be seen that all the points with reduced titin stiffness lie below the control curve, and their linear fit has a slightly increased slope (0.17 s, r = 0.98) compared to control (0.15 s, r = 0.97), a behavior similar to the condition of titin degradation by trypsin digestion (Fig. 7 of Helmes *et al.* [8]). Changing the ordinate to $dL/dt_{max}$ as a function of $SL_{PC}$ (Fig. S6B), simulation results also resemble the experimental PKA effect on restoring force (Fig. 6 of Fukuda *et al*. [9]), though the slope decrease is not as marked as found in rat myocytes (6.15 $s^{-1}$, r = 0.97 in control and. 5.75 $s^{-1}$, r = 0.98 in ISO vs. ~9 and ~7.5, respectively, in Fukuda´s study).

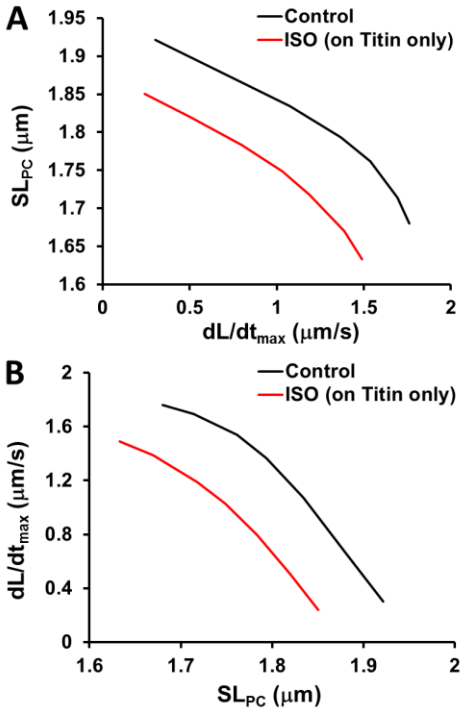


**Fig. S6**. Simulations of restoring force.

## *Length Step during Contraction*

A classical observation by Allen and Kurihara [10] was that a quick length step during an isometric contraction can cause release or decrease of $[Ca^{2+}]_i$ due to abrupt changes in myofilament $Ca^{2+}$ binding. Fig. S7 shows a simulation of that type of experiment. As can be seen, shortening of the SL caused a bump in $[Ca^{2+}]_i$ that was produced by the intrinsic effect of SL on myofilament $Ca^{2+}$ affinity in our model.

## *CaMKII effects during acute ISO application*

The model we use inherently includes both PKA and CaMKII signaling. Since CaMKII is known to have many targets in cardiac myocytes and can be activated downstream of β-AS [2] Fig. S8 shows the same 100 nM [ISO] simulation as in Fig. 7 with the normal model and with CaMKII changes disabled (CaMKII-clamp). While there are some minor differences that would be attributable to CaMKII, these would not appreciably alter any of the conclusions in the present study with respect to PKA effects on the targets addressed.

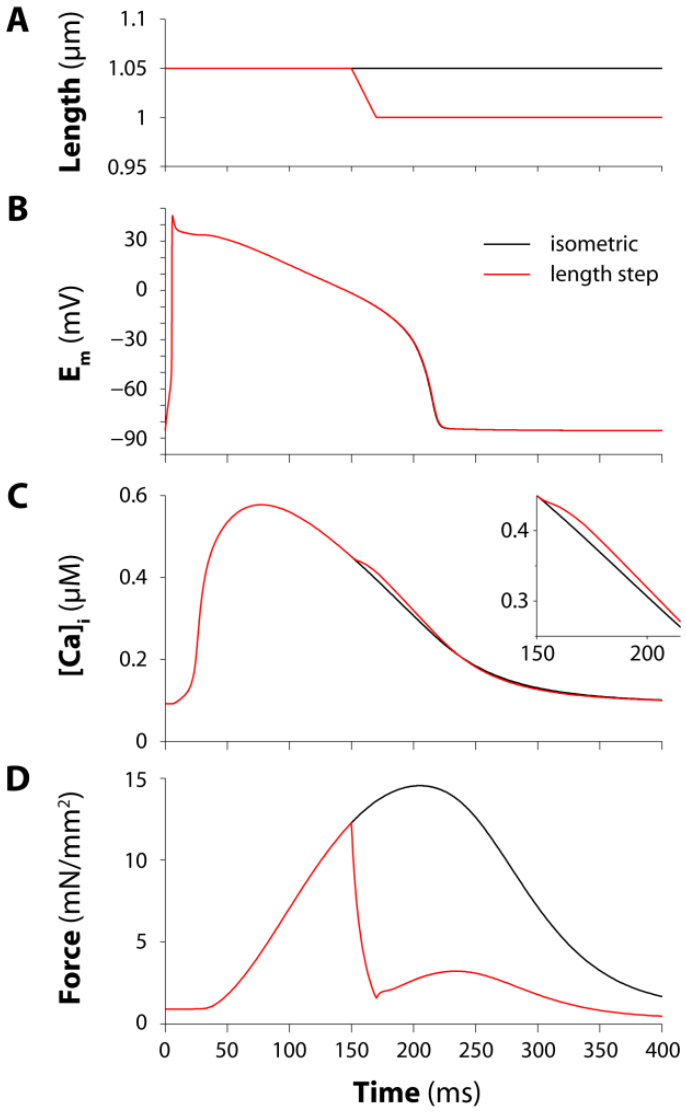


**Fig. S7**. Length step during contraction.

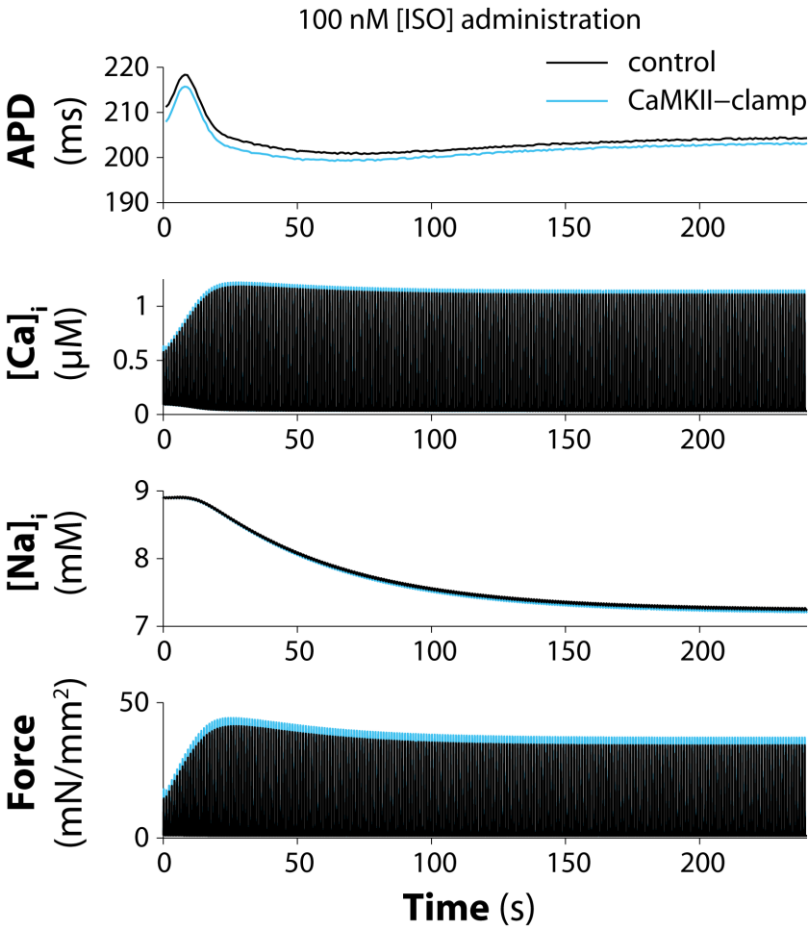


**Fig. S8**. Application of 100 nM [ISO] with normal model or with the CaMKII activation state clamped at the initial value. Black traces are the same as in Fig. 7.

## *Supplemental References*

[1] Granzier H, Helmes M, Trombitas K. Nonuniform elasticity of titin in cardiac myocytes: a study using immunoelectron microscopy and cellular mechanics. *Biophys J*. 1996;70:430-42.

[2] Soltis AR, Saucerman JJ. Synergy between CaMKII substrates and beta-adrenergic signaling in regulation of cardiac myocyte $Ca^{2+}$ handling. *Biophys J*. 2010;99:2038-47.

[3] Yang JH, Saucerman JJ. Phospholemman is a negative feed-forward regulator of $Ca^{2+}$ in beta-adrenergic signaling, accelerating beta-adrenergic inotropy. *J Mol Cell Cardiol*. 2012;52:1048-55.

[4] Xie Y, Grandi E, Puglisi JL, Sato D, Bers DM. beta-adrenergic stimulation activates early afterdepolarizations transiently via kinetic mismatch of PKA targets. J Mol Cell Cardiol. 2013;58:153-61.

[5] Xie Y, Grandi E, Bers DM, Sato D. How does beta-adrenergic signalling affect the transitions from ventricular tachycardia to ventricular fibrillation? *Europace*. 2014;16:452-7.

[6] Shannon TR, Wang F, Puglisi J, Weber C, Bers DM. A mathematical treatment of integrated Ca dynamics within the ventricular myocyte. *Biophys J*. 2004;87:3351-71.

[7] Weber CR, Piacentino V, 3rd, Ginsburg KS, Houser SR, Bers DM. $Na^{+}$-$Ca^{2+}$ exchange current and submembrane [Ca(2+)] during the cardiac action potential. *Circ Res*. 2002;90:182-9.

[8] Helmes M, Lim CC, Liao R, Bharti A, Cui L, Sawyer DB. Titin determines the Frank-Starling relation in early diastole. *J Gen Physiol*. 2003;121:97-110.

[9] Fukuda N, Wu Y, Nair P, Granzier HL. Phosphorylation of titin modulates passive stiffness of cardiac muscle in a titin isoform-dependent manner. *J Gen Physiol*. 2005;125:257-71.

[10] Allen DG, Kurihara S. The effects of muscle length on intracellular calcium transients in mammalian cardiac muscle. *J Physiol*. 1982;327:79-94.